



Dilute Pd₃Co₉₅₀ alloy encapsulated in defect- and N-rich carbon nanotubes for universal highly efficient aqueous-phase catalysis

Haifeng Yuan^a, Mei Hong^{a,*}, Feng Dong^a, Yanpeng Chen^b, Xinjuan Du^a, Xianzhen Huang^a, Jinqiang Gao^{a,*}, Shihe Yang^{a,c,**}

^a State Key Laboratory of Chemical Oncogenomics, Guangdong Provincial Key Laboratory of Nano-Micro Materials Research, School of Chemical Biology & Biotechnology, Peking University Shenzhen Graduate School (PKUSZ), Shenzhen 518055, PR China

^b Shenzhen Key Laboratory of Organic Pollution Prevention and Control, Environmental Science and Engineering Research Center, Harbin Institute of Technology (Shenzhen), Shenzhen 518055, PR China

^c Institute of Biomedical Engineering, Shenzhen Bay Laboratory, Shenzhen 518055, PR China



ARTICLE INFO

Keywords:

PdCo dilute alloy

N-rich carbon

Mott-Schottky heterojunction

Metal-N_x coordination

Aqueous-phase catalysis

ABSTRACT

Integration of dilute alloy with Mott-Schottky heterojunction has been achieved in porous sea-urchin-like N-rich carbon (CN) encapsulated Pd₃Co₉₅₀ alloy. Simply prepared through ZIF-67@C₃N₄ pyrolysis and trace Pd doping, the Pd₃Co₉₅₀@CN catalyst possesses dispersed high-electron-density Pd with electrons transferring from base Co and outer CN. Thanks to the enhanced metal-N_x coordination and discrete active surface Pd on Co, it displays excellent turnover frequency of 1656 h⁻¹ for cinnamaldehyde hydrogenation of C=C group with ~100% selectivity, and remarkable substrate tolerance in catalyzing various environmentally benign reactions in water, including hydrogenation of *N*-heterocycles and oxidation of benzyl alcohol. An array of experimental and theoretical studies, including *in-situ* characterization, kinetic analysis, and DFT calculations verify that the extraordinary performance is mainly attributed to the bimetallic electronic synergy and strong coordination with CN support. This facile synthesis strategy incorporates bimetallic synergy, strong support coordination, and optimized microstructure, thus enabling universality of cost-effective multifunctional catalysts.

1. Introduction

Transition-metal (TM) catalysts, possessing incompletely filled *d*-orbitals that easily donate and accept electrons, are indispensable in modern organic synthesis. Compared with homogenous catalysts, supported heterogeneous TM catalysts offer advantages of being stable and readily separable from the reaction mixture, but suffer from insufficient atom efficiency and low selectivity [1]. Ingenious ways to boost structural and electronic synergies include fabricating dilute bimetallic alloyed clusters or nanoparticles (NPs) and utilizing Mott-Schottky effect with functional doping of the support [2], [3]. Confining isolated metal atoms or clusters in crystalline porous materials could further overcome the shortcomings of traditional heterogenous catalysis giving rise to sinter-resistant catalysts with boosted activity and selectivity [4].

Among TM catalysts, Pd is dominating because of its high reactivity and functional group tolerance in various reactions [5]. However, the

high cost of Pd and propensity to agglomerate under harsh reaction conditions limit its use. The single atom catalysts (SAC) and single atom alloys (SAA), with maximized atom utilization efficiency, can minimize the use of noble metals while at the same time exhibiting extraordinary catalytic activity [6], [7]. A variety of metal combination with minority Pd has been explored, including PdCu, PdAg, and PdAu which present significantly reduced use of precious Pd metal [8], [9]. Supporting, preferably encapsulating, dilute Pd-based alloy on a porous substrate provide an important step in advancing the composite catalysts towards industrial applications. Currently, the support materials for dilute alloys are mostly metal oxides [2], which promote mass transport and enhance metal stability. On the other hand, although mesoporous N-doped carbon materials have demonstrated extreme efficiency in supporting metal catalysts with both excellent activity and stability [10], they have never been reported for anchoring dilute alloys in the scope of our knowledge. Incorporation of N doping in carbon materials leads to vacancies and

* Corresponding authors.

** Corresponding author at: State Key Laboratory of Chemical Oncogenomics, Guangdong Provincial Key Laboratory of Nano-Micro Materials Research, School of Chemical Biology & Biotechnology, Peking University Shenzhen Graduate School (PKUSZ), Shenzhen 518055, PR China.

E-mail addresses: hongmei@pku.edu.cn (M. Hong), jinqiang.gao@pku.edu.cn (J. Gao), chsyang@pku.edu.cn (S. Yang).

defects, affording abundant coordination sites due to enhanced electron transfer from electronic metal-semiconductor interactions, known as the Mott-Schottky effect which renders heterogenous support similar roles as ligands in homogeneous catalysts [11]. Besides, the hierarchical porous geometry such as carbon nanotube (CNT) structure entails a significant confinement effect on the entrapped metals [12]. We envision that synchronous achievement of these contributing factors will be highly beneficial for achieving superior multifunctional activity. By modulating interactions of trace Pd with base metal host and the porous semiconductive support, the geometric and electronic structures of the isolated minority metal species can be tuned, which endorses high catalytic activity and reaction generality.

Herein, we report novel embedment of dilute PdCo alloy nanocrystals in a sea-urchin-like N-doped hierarchical carbon network (CN) facilely prepared from ZIF-67@C₃N₄ as precursor. The majority host Co comes directly from the node metal of ZIF-67 while C₃N₄ acts as promoter strengthening electron transfer at the metal/N-doped carbon interface and pore template. Benefiting from the synergy between Pd-Co bimetallic active sites and the N-rich carrier, as well as the hierarchical CNT assembled support, the composite Pd₃Co₉₅₀@CN nano-catalysts, at ultralow Pd loading of 0.18 wt%, exhibit greatly enhanced aqueous-phase hydrogenation and oxidation reactions with excellent activity, selectivity, wide substrate tolerance, and stability.

2. Experimental

2.1. Chemicals and materials

All reagents were utilized as received without further purification, and ultrapure water (>18.2 MΩ) was used in all work. Details could be found in [Supporting Information](#).

2.2. Synthesis of ZIF-67@C₃N₄, Co@CN, and Pd_xCo_y@CN

Graphitic carbon nitride (C₃N₄) was prepared by thermal polymerization of urea. Typically, Urea (6.0 g) in a silica crucible (50 mL) was directly heated inside a muffle furnace from 20 °C to 550 °C with 5 °C min⁻¹ and kept at 550 °C for 4 h under air atmosphere. The obtained C₃N₄ was cooled to ambient temperature. To synthesize ZIF-67@C₃N₄, 0.45 g cobalt nitrate hexahydrate and 0.2 g C₃N₄ were dissolved in 40 mL methanol, labeled as solution A. Solution B was prepared by dissolving 5.5 g of 2-methylimidazole in 40 mL methanol. Solution B was slowly poured into solution A under constant magnetic stirring at 1500 rpm for 24 h at ambient temperature. The purple-colored product was washed with methanol five times and collected by centrifugation at 8000 rpm, and dried in a vacuum oven at 60 °C overnight.

The as-synthesized ZIF-67@C₃N₄ was placed in a ceramic boat (20 mL) and directly heated inside a tubular furnace from 30 °C to 750 °C with 2.5 °C min⁻¹ under 5 vol% H₂/Ar flow. After being held at 750 °C for 2 h, the boat was cooled down naturally and the obtained black Co@CN were collected. The bimetallic Pd_xCo_y@CN catalysts were prepared according to the procedure as follows: 0.5 g Co@CN, 20 mL acetone, and 60 mL n-hexane were added into a 100 mL beaker. After 3.0 h vigorous magnetic stirring to disperse the suspension, a required quality of palladium (II) nitrate was added, followed by constant stirring for 12 h at 1000 rpm. The obtained precipitates were collected by centrifugation (8000 rpm, 6 min), washed thoroughly with ultrapure water, and dried in a vacuum oven at 60 °C overnight, followed by treatment under 5 vol% H₂/Ar flow at 300 °C for 2 h. Different starting Pd-to-Co molar ratios of 3:950 and 10:950 were utilized and the acquired catalysts were represented as Pd₃Co₉₅₀@CN and Pd₁₀Co₉₅₀@CN, respectively. Pure ZIF-67 pyrolysis-derived support without C₃N₄, named as ZC, and the synthesis procedures for comparative samples of Pd_xCo_y/ZC can be found in [Supporting Information](#).

2.3. The catalytic reactions

Hydrogenation reactions were carried out in a 100 mL stainless steel autoclave. Calculated amounts of catalyst, reactant, and solvent were first added, then the autoclave was sealed and ventilated 3 times to exhaust air. Then hydrogen was introduced and the operation parameters such as temperature, pressure and reaction time were set. After the reaction, the product mixture was extracted with ethyl acetate for GC-MS (Agilent 8890–5977B) analysis to monitor conversion of reactants and selectivity of the target product, same as below. Thermodynamic behavior investigation on temperature effect was performed under a condition that limit the cinnamaldehyde (CAL) conversion to less than 20% by adjusting duration to reduce deviation in the measured reaction rate. The turnover frequency (TOF) value was calculated as the molar amount of CAL converted per mole of Pd metal sites per hour (mol_{CAL} mol⁻¹ h⁻¹) under the low conversion (<20%).

Oxidation reactions were carried out in an open-air two-necked flask with reflux condensation tube and without light exposure. First, calculated amounts of catalyst, reactant, and solvent were added. After reaching the set temperature, calculated amounts of hydrogen peroxide (30 wt%) was added dropwise. Sampling was performed at intervals. For the recyclability test, the used catalyst was recovered using an external magnet, washed thoroughly with ethyl acetate, and dried in a vacuum oven at room temperature for the next catalytic test. Methods for calculation of catalytic performance can be found in [Supporting Information](#).

2.4. Characterization of catalysts

The synthesized samples were characterized using an array of analytical methods. Raman spectra were recorded on a Horiba labRAM HR800 using a 532 nm He-Ne laser, were used to verify the degree of structural defects in the samples. Transmission electron microscopy (TEM) images were used to observe the morphology of various samples. Bruker multiMode-8AFM/SPM was used obtain atomic force microscope (AFM) images under environmental conditions using ScanAsyst mode. X-ray photoelectron spectroscopy measurements (XPS) were used to reveal the characteristic surface elemental compositions and electronic states of the samples. Diffuse reflectance infrared Fourier-transform spectroscopy (DRIFT) were used to obtain the adsorption characteristics of the sample for CO and cinnamaldehyde. Temperature-programmed reduction (TPR) and temperature-programmed desorption (TPD) of the samples were performed on a Micromeritics AutoChem II Model 2920 automated chemisorption instrument. Pd X-ray adsorption fine structure (XAFS) measurement was performed at the beam line BL14W1 of Shanghai Synchrotron Radiation Facility (SSRF), Shanghai Institute of Applied Physics (SINAP), Chinese Academy of Sciences (CAS). More on the different characterizations can be found in the [Supporting Information](#).

2.5. DFT calculation methods

Density functional theory (DFT) calculation were performed using the Vienna Ab-initio Simulation Package (VASP). The nonlocal exchange and correlation effects were described by the Perdew-Burke-Ernzerhof (PBE) form of generalized-gradient approximation (GGA) exchange-correlation energy function, in combination with DFT-D3 correction. The energy cutoff for the plane-wave basis was set to 400 eV. Structural optimizations were carried out by minimizing the forces on all atoms in the relaxed structures to less than 0.03 eV Å⁻¹ and the convergence tolerance of the energy was below 10⁻⁴ eV. The k-point spacing was set to be smaller than 0.03 Å⁻¹ over Brillouin zone (BZ). Details could be found in [Supporting Information](#).

3. Results and discussion

3.1. Synthesis and structural characterizations

The formation pathway of $Pd_xCo_y@CN$ is displayed in Fig. 1a, where x and y represent the molar ratio of Pd and Co in the precursor mixture. First, ZIF-67@ C_3N_4 was synthesized verified by SEM-EDX and C-N content (Fig. S1), XRD patterns and FT-IR spectra (Fig. S2), XPS spectra (Fig. S3), and N_2 adsorption-desorption isotherms (Fig. S4). Then the ZIF-67@ C_3N_4 composite was pyrolyzed into porous sea-urchin-like Co@CN with Co particle size about 11.3 nm (Fig. S5). Since C_3N_4 can be completely decomposed before 710 °C manifested in the TGA curves (Fig. S6), we chose pyrolysis at 750 °C. Last, impregnation of Pd cations were conducted on Co@CN, forming $Pd_xCo_y@CN$. As shown in Fig. 1(b, c), $Pd_3Co_{950}@CN$ retains the original shape of Co@CN. The nanotubes are highly dispersed with bamboo-shaped outline and encapsulated NPs (Fig. 1d). High resolution TEM image (HRTEM, Fig. 1e) reveals a typical graphite interlayer spacing of 3.58 Å. The average size of highly dispersed metals is about 12.9 nm (Fig. 1 f). A closer look of a tip-embedded single particle (Fig. 1 g) displays an obvious wrapped structure with metal NP core and N-doped carbon shell. The lattice spacing of (111) plane for the PdCo alloy (Fig. 1 h) is 2.08 Å, in between the d-spacing values of pure Pd (2.25 Å) and Co (2.04 Å) [13]. Sharp contrasted strain maps (Fig. 1 i) indicating strong interactions within the bimetallic NPs. The selected area electron diffraction (SAED) pattern (Fig. 1 j) agrees with the polycrystalline PdCo crystals and amorphous carbon. Meantime, HAADF-STEM and elemental profiles (Fig. 1 k) verify the presence of atomic-level Pd within bimetallic NPs. The trace doping of 0.18 wt% Pd in $Pd_3Co_{950}@CN$ is confirmed by EDS (Fig. S7) and ICP (Table S1), and the loading efficiency was calculated to be 72%.

Vital effects of C_3N_4 were systematically discussed. With a N content of 57.9 wt% (Fig. S1h), the C_3N_4 pyrolysis could produce a large number of N-rich motifs, which provides abundant reactive sites [14]. When the precursor material was only ZIF-67, the synthesized Pd_3Co_{950}/ZC sample basically retained the smooth dodecahedron structure without nanotubes (Fig. S8). The PdCo NP size in Pd_3Co_{950}/ZC was averaged at 21.2 nm, larger than that in $Pd_3Co_{950}@CN$, probably due to the lack of CNT confinement effect [15]. Meantime, the preferred $Pd_3Co_{950}@CN$ exhibits larger BET surface area ($579\text{ m}^2\text{ g}^{-1}$) compared to Pd_3Co_{950}/ZC (Fig. S9). The high porosity of interweaving carbon nanotube network templated by C_3N_4 promotes the exposure of active sites for boosting mass transfer [16]. It is noteworthy that the presence of Co is indispensable for inducing carbon nanotube. No carbon nanotubes were produced when ZIF-8 was used instead of ZIF-67 (Fig. S10). Therefore, the Co species promoted C_3N_4 pyrolysis into N-rich CNT, while C_3N_4 transformed ZIF-67 into 3D graphitic carbon network [17], [18]. To more clearly reveal the effective growth of PdCo dilute alloy incorporated in $Pd_xCo_y@CN$, we changed the Pd doping amount from 0.18 wt% to 0.68 wt%, forming $Pd_{10}Co_{950}@CN$ (Fig. S11). Unsurprisingly, the $Pd_{10}Co_{950}@CN$ sample shows similar morphology but bigger NP size (17.8 nm). With increased Pd doping, the lattice spacing gradually shifts to bigger value since the lattice constant of Pd is larger than that of Co [19].

The XRD peaks at 44.3° and 51.4° (Fig. S12) prove that Co exists in the fcc-structured metallic (PDF#15–0806) instead of oxide form. Raman spectra show (Fig. S13) two peaks at about 1360 and 1590 cm⁻¹ that correspond to the D band reflecting disordered carbon defects and the G band reflecting graphite structure with E2g symmetry [20]. Adding C_3N_4 and incorporating atomic-level Pd contribute to the enhanced $I_D:I_G$ ratio with reduced graphitization degree, rendering a higher carbon defect density and more active sites [21]. Therefore, $Pd_3Co_{950}@CN$ has the highest $I_D:I_G$ ratio reaching 2.9. The significant differences are complementarily analyzed by XPS (Fig. 2(a-c) and Table S2). In the N 1s spectra, the two different peaks at approximately 396.9 eV and 401.0 eV can be attributed to pyridinic and graphitic N, respectively [22]. Co@CN has higher graphitic N content than the two

$Pd_xCo_y@CN$ samples, suggesting that trace Pd addition could suppress graphitization. Meanwhile, the binding energy (BE) of $Pd_3Co_{950}@CN$ shifts to a higher value compared to Co@CN and Pd_3Co_{950}/ZC , indicating that the N species imparted by C_3N_4 allow tighter coordination with Pd_xCo_y dilute alloy (Fig. S14) [23]. Consistent with the highest $I_D:I_G$ ratio, $Pd_3Co_{950}@CN$ has the highest ratio of pyridinic N, and its value decreased with increased Pd doping. The Co 2p_{2/3} XPS spectra can be deconvolved into Co^0 (~778 eV), $Co-N_x$ (~780 eV), and satellite peaks (~787 eV). The $Pd_3Co_{950}@CN$ sample exhibits the highest $Co-N_x/(Co-N_x+Co^0)$ ratio with increased BE of Co^0 , indicating stronger interaction between Co and N owing to electron transfer between Pd and Co [24]. No oxidized high valent Co species were observed thanks to the strong bimetallic interactions and the tight encapsulation by the N-doped carbon (CN) shell, preventing oxidation. The protective role of CN on PdCo alloy was further confirmed by higher temperature pyrolysis at 950 °C (defined as $Pd_3Co_{950}@CN-950$, Fig. S15), the PdCo NP only slight increased to 28.3 nm, thus CN nanotube shells enhance the stability of the catalyst structure. The Pd 3d XPS data show weak signals (Fig. S16), which may be attributed to the trace Pd content within the ultra-dilute alloy and the N-rich carbon-encaged structure [25]. As the binding energy apparently shifts in the N 1s and Co 2p XPS spectra verifying interactions of the surface Pd atoms with both N and Co in the sample, the Pd 3d region peaks could be arising from metallic, N-coordinated, and charged states. Deconvolution fitting results following previous method [26] indicate that $Pd_3Co_{950}@CN$ possesses the highest $Pd-N_x/(Pd^0+Pd-N_x+Pd^{2+})$ ratio, confirming the strongest coordination between pyridinic N and Pd in $Pd_3Co_{950}@CN$ by Mott-Schottky effect at the Pd-N-C interface likely related to the ultrafine size of Pd [27].

In-situ DRIFTS of CO adsorption (Fig. 2(d-g)) reveals the highly dispersed Pd active sites with enhanced electron transfer of $Pd_3Co_{950}@CN$. Generally, the below 2000 cm⁻¹ bands correspond to multi-coordinated adsorption of CO on metal atoms while above 2000 cm⁻¹ bands correspond to linear adsorption [28]. For Co@CN (Fig. 2d), adsorption band at 1791 cm⁻¹ can be ascribed to the tri-coordinated CO adsorbed on 3-fold site [29], and those at 2001 cm⁻¹ and 2052 cm⁻¹ are dominated by the linear adsorption on Co [28], [30]. These linear CO adsorption peaks are present in all samples. Compared to the monometallic Co@CN samples, the three bimetallic samples containing trace Pd exhibit blue-shift of the peak position. With the introduction of Pd, the lower electron density of Co reduces the electron feedback from the d orbital of Co to the π^* orbital of CO [31], [32]. The $Pd_3Co_{950}@CN$ sample shows the most significant shifts toward higher wavelengths of 2013 cm⁻¹ and 2063 cm⁻¹, verifying the weakest absorption for CO (Fig. 2e). Stemming from the highly diluted nature of Pd, linear CO adsorption on the low coordination edges or corner sites of atomic-level Pd give rise to the 2041 cm⁻¹ band [33]. In the meantime, competitive adsorption of CO on the dispersed Pd sites versus the Co sites leads to suppression of the multi-coordinated CO signals on Co site at around 1800 cm⁻¹ upon bimetallic alloying [29], [34], further suggests the atomic-level Pd distribution on the Co NP surface. With increasing Pd ratio, the appearance of bridging signals at 1965 cm⁻¹ for $Pd_{10}Co_{950}@CN$ sample (Fig. 2f) suggest Pd aggregation [35], consistent with TEM observations. Also, the linear CO adsorption at higher wavenumber at approximately 2072 cm⁻¹ can be attributed to the higher Pd⁰ BE of $Pd_{10}Co_{950}@CN$ relative to $Pd_3Co_{950}@CN$ (Table S2) [32], [36]. It has been reported that having atomic-level Pd leads to a reduction in Pd⁰ BE binding energy [37]. The Pd_3Co_{950}/ZC sample (Fig. 2g) also show bridged adsorption of CO on Pd at 1973 cm⁻¹ indicating Pd particle properties [35]. Furthermore, the in-situ CO-DRIFTS of Pd@CN (Fig. S17a) shows tricoordinated CO adsorbed on 3-fold Pd at 1859 cm⁻¹ and bridged CO adsorption at 1982 cm⁻¹, verifying the large Pd ensembles [38], [39], consistent with TEM observations (Fig. S17(b, c)).

To further support the above analysis, the atomically dispersed Pd sites in the samples were further analyzed by X-ray absorption near-edge structure (XANES) spectroscopy. Likely due to the low Pd loading of 0.18 wt% and the influence of Co content up to 34.13 wt%, the XANES

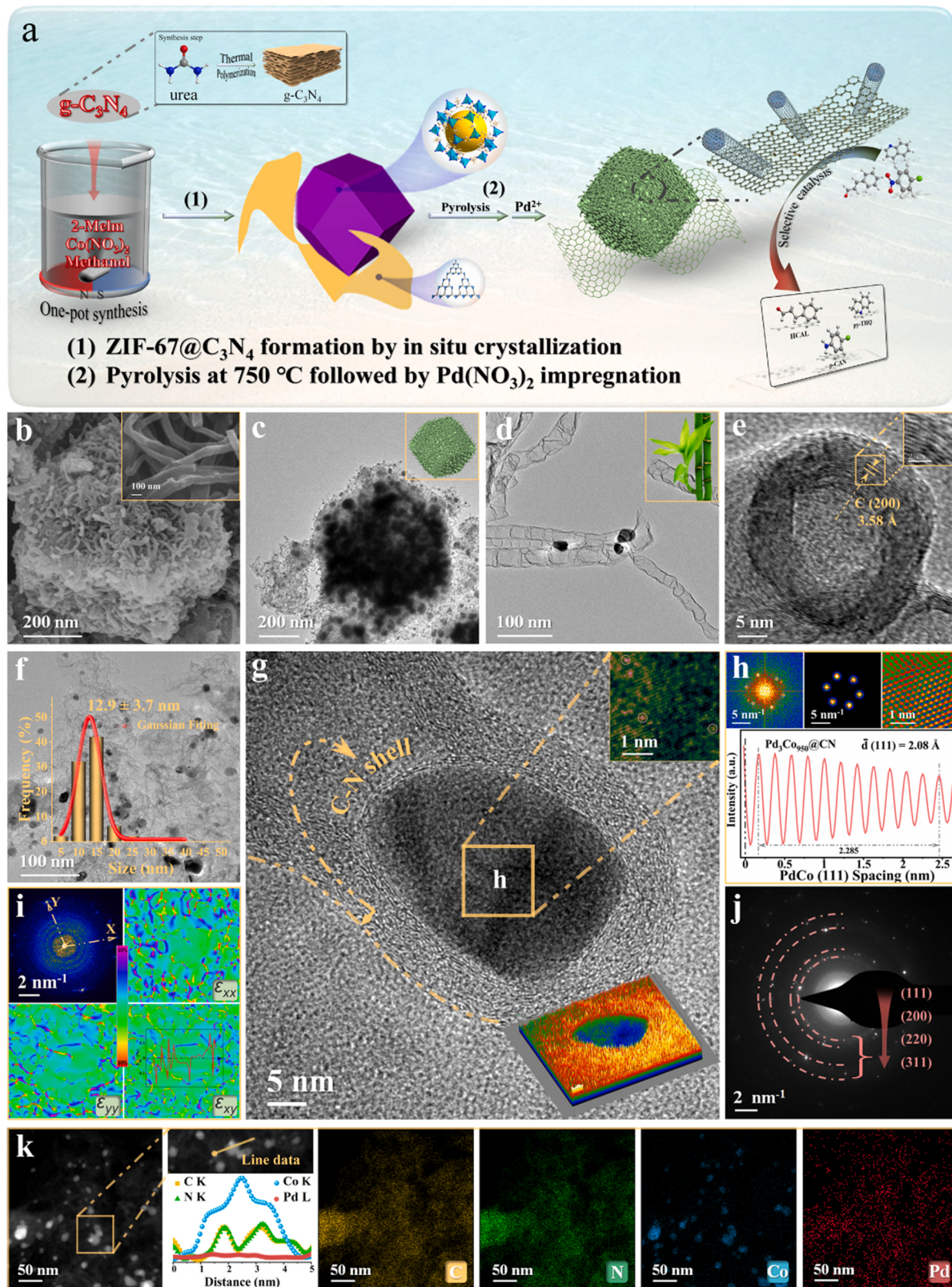


Fig. 1. Synthesis and characterizations of Pd₃Co₉₅₀ @CN. (a) Schematic illustration of the fabrication process. (b) SEM. (c-f) TEM images, inset in (b) shows the nanotubes, in (c) is a cartoon illustration of the composite containing dispersed metal within nanotube and mesoporous N-doped carbon matrix, in (d) a bamboo-like nanotube, in (e) enlarged HRTEM, and in (f) the NP size distribution, respectively. (g) HRTEM images of single NP. (h) The corresponding inverse FFT patterns. (i) Strain maps of tensors ε_{xx} , ε_{yy} , and ε_{xy} processed by GPA. (j) SAED pattern. (k) HAADF-STEM image with elemental line-scanning profiles along the direction marked by an orange line, and the corresponding EDS mappings.

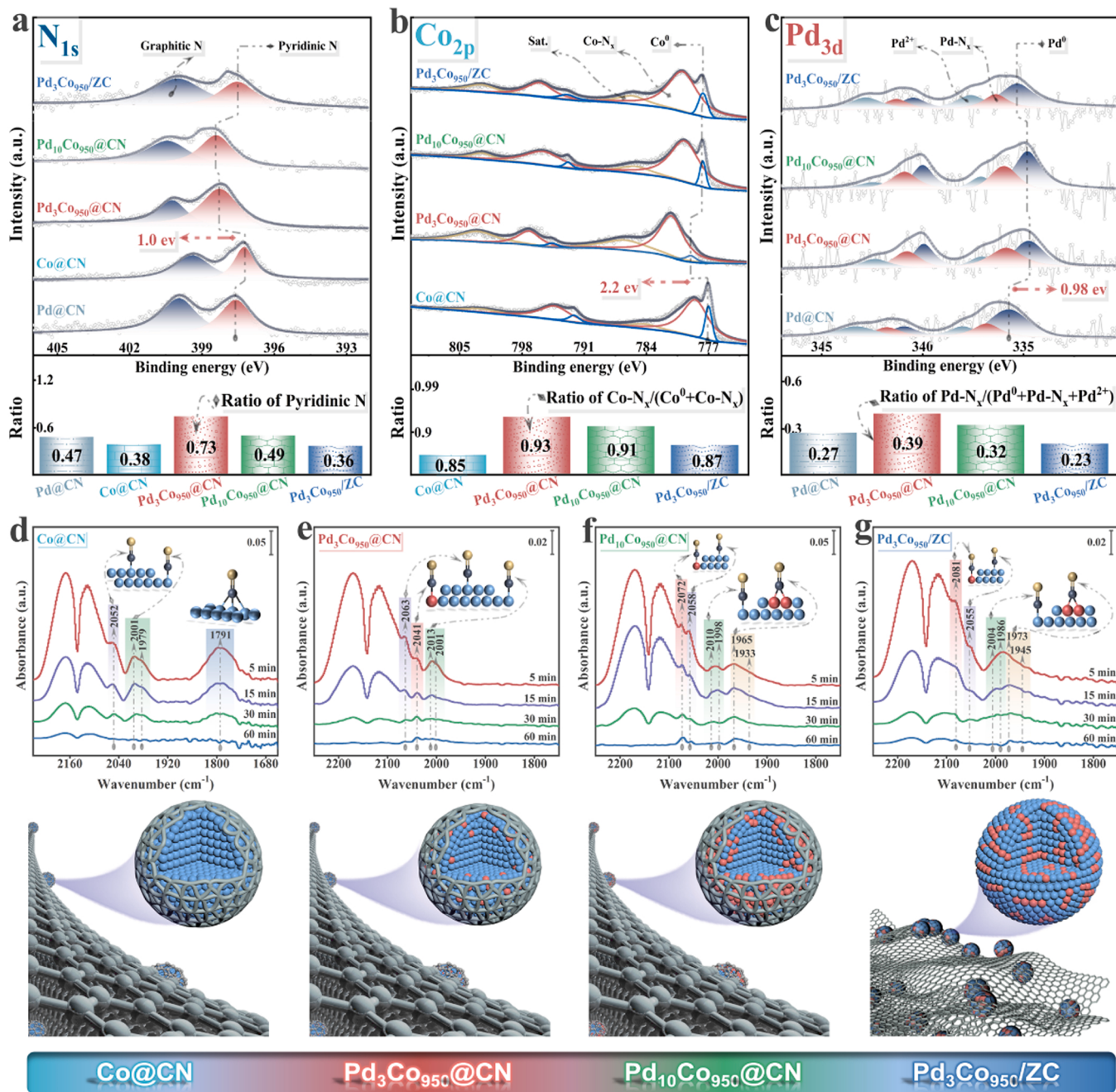


Fig. 2. Comparative characterization of various catalysts. (a) N 1s XPS spectra. (b) Co 2p XPS spectra. (c) Pd 3d XPS spectra. In-situ DRIFTS of CO adsorption on the catalysts with 3D structures: (d) Co@CN; (e) Pd₃Co₉₅₀@CN; (f) Pd₁₀Co₉₅₀@CN; (g) Pd₃Co₉₅₀/ZC. Co: blue; Pd: red; C: gray; O: yellow.

spectra of Pd₃Co₉₅₀@CN and the corresponding extended X-ray absorption fine structure (EXAFS) oscillations are noisy (Fig. S18), which prevents further data analysis using Athena software. The quality of X-ray absorption spectroscopy (XAS) spectra of the target element is affected by their own content and easily interfered with by the presence of co-existing elements [40], [41]. The higher Pd content (0.68 wt%) sample of Pd₁₀Co₉₅₀@CN gives observable XANES spectra (Fig. S19a) with the Pd K-edge absorption energy close to that of Pd foil but much below that of PdO, indicating that the system is Pd⁰-rich, which is in accordance with the XPS results [42]. The EXAFS spectrum (Fig. S19b) of Pd₁₀Co₉₅₀@CN exhibits a stronger shoulder peak located at ~2.6 Å, which is in the region between Pd-N shell (1.5 Å) and Pd-Pd shell (2.7 Å) and can be assigned to the Pd-Co coordination. The EXAFS data-fitting (Fig. S20 and Table S3) result in a Pd-Co coordination number of 1.1

± 0.2 and Pd-Pd of 6.6 ± 0.3, much lower than those of typical FCC bulk and surface (111) coordination numbers of 12 and 9. This confirms the formation of PdCo alloy and Pd atoms are incorporated on/near the surface with dangling bonds [25]. Therefore, Pd₁₀Co₉₅₀@CN may be a mixed phase consisting of atomic-level Pd and Pd nanoparticles, which is consistent with the conclusions reached by the HAADF-STEM images and in-situ CO-DRIFTS data. With the decrease of Pd loading, based on the conclusions reached by the in-situ CO-DRIFTS, it is expected that the Pd species on Co NPs would further change from few-atom Pd cluster to monodisperse state containing atomically dispersed Pd sites. Notably, the peak of Pd-N coordination confirms the interaction of Pd with nitrogen-doped carbon (CN) shell, and the EXAFS spectra also clearly show that Pd-O bonds are not present. The close interaction of surface Pd atoms with N in the CN shell forming the Pd-N coordination further

supports the presence of isolated Pd sites.

3.2. Catalytic performance

The hydrogenation reaction of cinnamaldehyde was employed to compare the catalytic performance of the different catalysts of interest in this study. CAL hydrogenation is one of the most important reactions in the production of basic organic intermediates widely used in

pharmaceutical, agrochemical and perfume industries [43]. However, due to conjugation between C=O and C=C bonds, so far, effective and selective CAL hydrogenation is still a huge challenge often resulting in slow reaction and mixture products (Fig. S21) [44]. Herein, efficient and low-cost $\text{Pd}_3\text{Co}_{950}@\text{CN}$ catalyst was developed which showed high activity, selectivity and maximized utilization of metal atoms (Fig. 3a). Under the environmentally benign mild aqueous condition in 5 bar H_2 at 50 °C, $\text{Pd}_3\text{Co}_{950}@\text{CN}$ showed 93.6% CAL conversion and ~100%

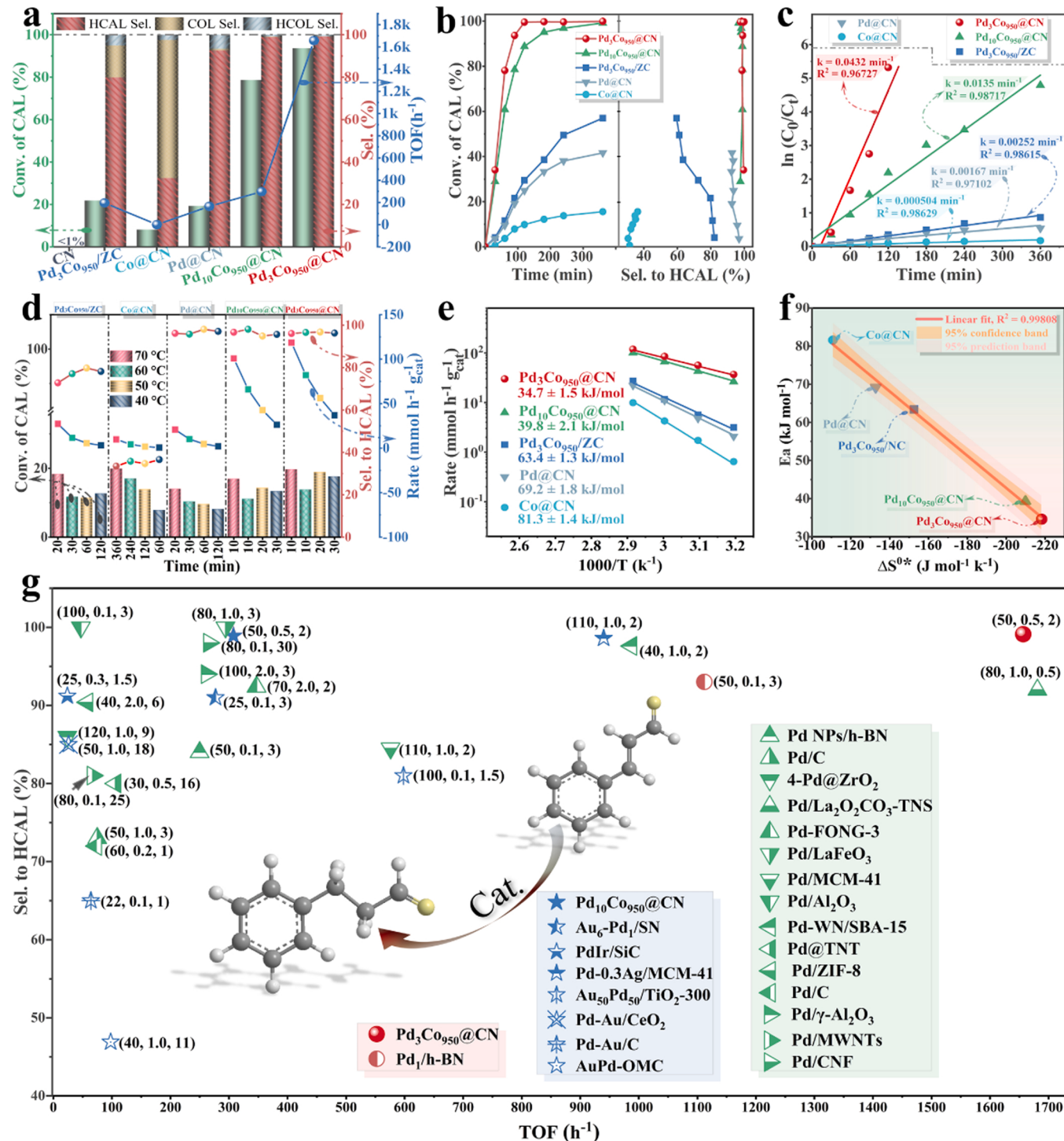


Fig. 3. Performance evaluation of CAL hydrogenation with several representative catalysts: (a) Conversion and selectivity (reaction conditions: 50 °C; 5 bar H_2 ; 800 rpm; S/C = 2661; 10 mL water; 1.5 h). (b) Kinetic profiles. (c) Plot of $\ln(C_0/C_r)$ vs. time. (d) Effect of reaction temperature. (e) Arrhenius plots. (f) Plot of activation energy (E_a) against entropy change ($\Delta S^{\circ*}$). (g) Comparison of selectivity-TOF trade-off (the values in brackets refer to the reaction temperature (°C), H_2 pressure (MPa), and time (h), see Table S4 for details).

hydrocinnamaldehyde (HCAL) selectivity, outperforming bimetallic $\text{Pd}_{10}\text{Co}_{950}@\text{CN}$ and $\text{Pd}_3\text{Co}_{950}/\text{ZC}$, monometallic $\text{Co}@\text{CN}$, $\text{Pd}@\text{CN}$, and commercial Pd/C (Fig. S22). The $\text{Pd}_3\text{Co}_{950}@\text{CN}$ exhibited the highest TOF of 1656 h^{-1} , sixfold that of 298 h^{-1} using $\text{Pd}_{10}\text{Co}_{950}@\text{CN}$ with almost identical ~99% HCAL selectivity, confirming the beneficial effect of ultra-dilute alloy with atomically dispersed active sites. Also they are far higher than that of 196 h^{-1} using pyridinic N-poor $\text{Pd}_3\text{Co}_{950}/\text{ZC}$ with only 79.8% HCAL selectivity, confirming the positive effect of enhanced electron transfer at the metal/N-doped carbon interface.

In previous studies, the hydrogenation performance of CAL could be adjusted by metal particle size [45], the type and density of defects [46], [47], and the interaction between metallic sites [48]. In this study, the preferred $\text{Pd}_3\text{Co}_{950}@\text{CN}$ catalyst showed the best hydrogenation performance due to the electronic effect between Pd-Co and the Mott-Schottky effect from metal/N-doped carbon matrix, synergistically contributing to the highest *d*-band electron cloud density at Pd which in turn leads to its excellent activity [49]. Further kinetic study reveals first-order rate constant by $\text{Pd}_3\text{Co}_{950}@\text{CN}$, 0.0432 min^{-1} , orders of magnitude higher compared with reference catalysts (Fig. 3(b, c)). The constant reaction rate with respect to stirring speed and concentration (Fig. S23) confirmed the absence of external diffusion and mass transport influences. The lowest activation energy E_a of 34.7 kJ mol^{-1} and the largest apparent entropy change ΔS^{0*} of $-218.2 \text{ J mol}^{-1} \text{ K}^{-1}$ for $\text{Pd}_3\text{Co}_{950}@\text{CN}$ (Fig. 3(d, e), S24) indicate that the surface atoms have a more suitable adsorption effect on the adsorbate [50]. Of note, the uneven surface of $\text{Pd}_3\text{Co}_{950}@\text{CN}$ can be visually observed by atomic force microscopy (AFM, Fig. S25), which is beneficial for exposing more adsorption sites [51]. Excellent linear relationship between E_a and ΔS^{0*} (Fig. 3 f) confirms the compensation effect due to bonding between surface Pd atoms and the adsorbate [52]. The catalytic performance of $\text{Pd}_3\text{Co}_{950}@\text{CN}$ for CAL hydrogenation was compared with previously reported heterogeneous catalysts (Fig. 3 g), showing extraordinary

catalytic activity and excellent selectivity.

3.3. Recycling test and mechanistic study by chemisorption, *in-situ* IR

Increasing H_2 pressure promotes CAL conversion and slightly decreases HCAL selectivity (Fig. S26) due to formation of hydrocinnamyl alcohol (HCOL). Therefore, we choose 5 bar as the preferred pressure to ensure high HCAL yield. The plot of $\log(\text{P}(\text{H}_2))$ vs. reaction rate yields a slope of approximately 1 indicating that the reaction was of first-order relative to H_2 partial pressure. Owing to the excellent hydrophilicity of the preferred $\text{Pd}_3\text{Co}_{950}@\text{CN}$, the catalytic performance is superior in water than in organic solvents (Fig. S27), which is environmentally benign. The $\text{Pd}_3\text{Co}_{950}@\text{CN}$ catalyst is ferromagnetic with a saturation magnetization of 72.2 emu g^{-1} (Fig. 4a), showing easy recovery by an external magnetic field (Movie S1) and no active site leaching during catalysis (Fig. S28). It also exhibits remarkable reusability (Fig. 4b) maintaining excellent CAL hydrogenation after six uses with CAL conversion and HCAL selectivity all greater than 92.7%. In contrast, the activity of commercial Pd/C decreases gradually during usage. The catalyst stability can be explained by the textual and compositional properties of used catalysts revealed by ICP (Table. S1), N_2 adsorption-desorption isotherms (Fig. S29), XRD patterns (Fig. S30a), Raman spectra (Fig. S30b), and HR-TEM images (Fig. S31). With ferromagnetic behavior and unique electronic structure, $\text{Pd}_3\text{Co}_{950}@\text{CN}$ does not alter composition and structure properties of the active species during consecutive uses. In contrast, the Pd content of Pd/C decreases accompanied by obvious agglomeration. Moreover, the catalytic performance of $\text{Pd}_3\text{Co}_{950}@\text{CN}$ stored in air for 3 months was almost the same as that of fresh catalyst (Fig. S32).

To further reveal the underlying structure-activity relationships, we performed systematic characterizations consisting of H_2 temperature-programmed reduction ($\text{H}_2\text{-TPR}$, Fig. 4c), H_2 temperature-programmed

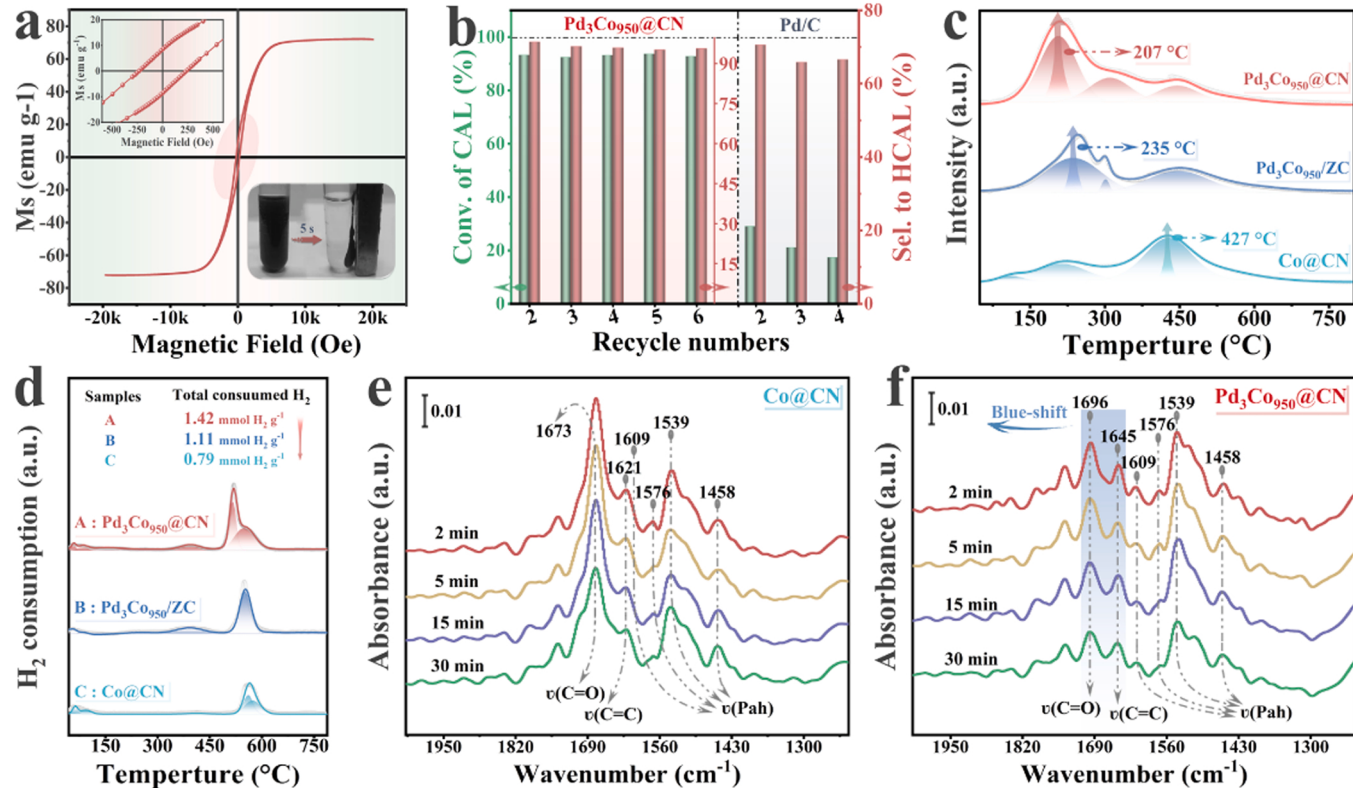


Fig. 4. (a) Magnetization curves at room temperature (Insets are magnified magnetic hysteresis loop from -600 to 600 Oe and photos of the sample from dispersed in ultra-pure water to under external magnetic field). (b) Reusability compared with Pd/C in the consecutive cycles. Reaction conditions: 50°C ; 800 rpm ; $\text{S/C} = 2661$; 10 mL water; 5 bar H_2 ; 1.5 h . (c) $\text{H}_2\text{-TPR}$ profiles. (d) $\text{H}_2\text{-TPD}$ profiles. (e, f) In-situ DRIFT spectra of CAL adsorption on (e) $\text{Co}@\text{CN}$ and (f) $\text{Pd}_3\text{Co}_{950}@\text{CN}$.

desorption ($\text{H}_2\text{-TPD}$, Fig. 4d), and operando DRIFT of CAL adsorption (Fig. 4(e, f)). The major reduction peak temperatures in $\text{H}_2\text{-TPR}$ profiles for bimetallic catalysts are ~ 200 °C lower than that of Co@CN thanks to the hydrogen spillover from Pd to the lower-coordinated Co. The higher N doping in $\text{Pd}_3\text{Co}_{950}\text{@CN}$ synthesized in the presence of C_3N_4 further lowers the reduction temperature and increases H_2 consumption confirming the beneficial effect of N-rich carbon defects and strong interactions of atomic-level Pd with low-coordinated Co [53]. This enhanced hydrogen spillover effect is supported by $\text{H}_2\text{-TPD}$ showing two main peaks [54], [55]. The low-temperature desorption peak < 200 °C attributes to the hydrogen chemisorbed on Co, while the high temperature desorption peak > 400 °C is caused by hydrogen desorption from Pd which overflows to the low-coordinated Co [56], [57]. Doping Pd significantly enhances hydrogen desorption, indicating that Pd is the site of H_2 adsorption and dissociation [58]. The peak H_2 desorption temperature is the lowest for $\text{Pd}_3\text{Co}_{950}\text{@CN}$ at ~ 520 °C. So, hydrogen species, readily adsorbed and dissociated on the dilute Pd sites with spillover to the adjacent Co, could reduce the formation of hydrogenated Pd species [59]. While $\text{H}_2\text{-TPR/TPD}$ confirms the enhanced hydrogen spillover, operando DRIFT of cinnamaldehyde verifies the weakened C=O adsorption. Compared with Co@CN (Fig. 4e), the adsorbed CAL on $\text{Pd}_3\text{Co}_{950}\text{@CN}$ displays obvious blue-shift for stretching vibration of C=O ($\nu(\text{C=O})$) from 1673 cm^{-1} to 1696 cm^{-1} , and for stretching vibration of C=C ($\nu(\text{C=C})$) from 1621 cm^{-1} to 1645 cm^{-1} [60], [61], while those for the characteristic vibrations of aromatic backbone at 1609 cm^{-1} , 1576 cm^{-1} , 1539 cm^{-1} , and 1458 cm^{-1} maintain at identical positions (Fig. 4f). Meanwhile, the peak intensity ratio of $\nu(\text{C=O})/\nu(\text{C=C})$ is lowered indicating that CAL interacts with the surface of $\text{Pd}_3\text{Co}_{950}\text{@CN}$ mainly through lay-flat C=C groups [29], [61]. With weakened C=O adsorption, $\text{Pd}_3\text{Co}_{950}\text{@CN}$ also shows a facile desorption with faster peak intensity attenuation than that of Co@CN.

3.4. Density functional theory calculations

To clarify the impacts of dilute alloy and Mott-Schottky effect, DFT calculations were performed. Based on the explicit geometric models of Co@CN and $\text{Pd}_3\text{Co}_{950}\text{@CN}$ (Fig. 5a), dilute alloy $\text{Pd}_3\text{Co}_{950}$ (111) has a significantly larger work function ($\varphi = 7.47\text{ eV}$) than nitrogen-doped carbon, CN (002) ($\varphi = 1.10\text{ eV}$) (Fig. 5b), verifying facile electron transfer from CN to $\text{Pd}_3\text{Co}_{950}$ at the Mott-Schottky interface [62]. The differential charge density analysis of $\text{Pd}_3\text{Co}_{950}\text{@CN}$ (Fig. 5c) shows obvious electron migration from the outer CN to the inner atomic-level Pd, which modulates electronic structure of the composite $\text{Pd}_3\text{Co}_{950}\text{@CN}$ catalyst [63]. To provide clear evidence about charge transfer, we performed a Bader charge analysis (Fig. S33) of $\text{Pd}_3\text{Co}_{950}\text{@CN}$. The amount of charge transferred from the outer CN shell to the inner Pd-Co dilute alloy is calculated to be 1.047 e , and the isolated Pd atom receives 0.43 e from sub-surface Co atoms, which is in line with the XPS and in-situ CO-DRIFTS results. Fig. 5d shows the density of states (DOS) around the Fermi level (E_F) before and after doping one Pd atom, and Fig. 5e displays the valence band (VB). The d -band center of $\text{Pd}_3\text{Co}_{950}$, $\sim -2.19\text{ eV}$, is farther from E_F , indicating a decrease in the antibond energy state as well as a weakening of the binding energy between catalyst and adsorbate [64], [65]. Furthermore, an N-deficient structural model (Fig. S34) confirms the positive effect of pyridine N species. Calculated free energies of hydrogen adsorption on $\text{Pd}_3\text{Co}_{950}\text{@CN}$, -2.64 eV , is much lower than that of -3.13 eV on Co@CN (Fig. 5 f). Thus, hydrogen adsorption/desorption on $\text{Pd}_3\text{Co}_{950}\text{@CN}$ is easier compared to Co@CN [66]. A small electron cloud formed between adsorbed H atom and the $\text{Pd}_3\text{Co}_{950}$ (111) (Fig. 5 g) would favor desorption of the H intermediate from catalyst surface. For CAL, $\text{Pd}_3\text{Co}_{950}\text{@CN}$ exhibits much higher adsorption energies than Co@CN (Fig. 5 h and Fig. S35). Furthermore, the bond length of C=C , which is 1.321 \AA in the gaseous CAL molecule, increased upon its adsorption onto Co@CN and $\text{Pd}_3\text{Co}_{950}\text{@CN}$ to 1.348 \AA and 1.361 \AA . The larger bond lengths on $\text{Pd}_3\text{Co}_{950}\text{@CN}$ than on Co@CN suggests prominently enhanced activation of C=C on the

ultra-dilute alloy through losing electrons [63], in comparison with the pristine Co (111). Correspondingly, the bond angle of C=C has increased (Fig. S36), further confirming that CAL tends to lie flat on the $\text{Pd}_3\text{Co}_{950}\text{@CN}$ surface.

Combining experimental characterizations and DFT calculation, the excellent activity and selectivity of $\text{Pd}_3\text{Co}_{950}\text{@CN}$ for CAL hydrogenation could be unambiguously ascribed to the synergistic ultra dilute alloying effect and the enhanced Mott-Schottky contact with N-rich carbon, as illustrated in the proposed mechanism (Fig. 5i). The electron-rich Pd can repel the adsorption of C=O bonds and promote the preferential flow of hydrogen molecules, generating a large number of surface-active H species. The Co-N_x sites act as a "reservoir" and "bridge" for the H species to spill over, while strengthening the activation of C=C bonds in the "lying" adsorption mode [67]. The CN shell as a P-type semiconductor with abundant positively charged pyridinic N facilitates CAL adsorption with π -electron-rich benzene ring [47]. With the insertion of activated hydrogen, the generated HCAL will be excluded from the support and replaced by a new CAL molecule.

3.5. Universality and scalability of $\text{Pd}_3\text{Co}_{950}\text{@CN}$

Due to the excellent performance of $\text{Pd}_3\text{Co}_{950}\text{@CN}$, we further investigated a wide scope of reactions, including selective hydrogenation (SH) of aldehydes, esters, *N*-heterocycles, ketones, nitroarenes, phenols and alkynes, as well as selective oxidation (SO) of benzyl ethanol (BnOH), fully proving its wide applicability. All reactions proceeded in water instead of typically employed organic solvents [68], confirming its environmental friendliness. As summarized in Fig. 6, Table S4-S5, the catalysis with $\text{Pd}_3\text{Co}_{950}\text{@CN}$ afforded the corresponding products with high yields ranging from 71.8% to 99.9%. Especially for the hydrogenation of *p*-chloronitrobenzene and *p*-nitrophenol, $\text{Pd}_3\text{Co}_{950}\text{@CN}$ displayed outstanding catalytic performance with yields of almost 100%. Even for phenylacetylene hydrogenation, 52.6% yield of styrene is realized. Under mild reactions, the selective hydrogenation of quinolines and a broad range of *N*-heterocycles with $> 90\%$ yields is highly desirable for its atom efficiency [69]. Furthermore, $\text{Pd}_3\text{Co}_{950}\text{@CN}$ selectively hydrogenate nitroarenes to the corresponding anilines with almost 100% yield which is advantageous as it does not require high-pressure hydrogen or hydrogen donor [70]. More universally, it also effectively catalyzed oxidation reactions. Using hydrogen peroxide as an oxidant, under atmospheric pressure, the BnOH oxidation selectively produced benzaldehyde (BzH) with 96.7% yield after 4 h at 100 °C, outperforming most supported metal catalysts. Excellent scalability of $\text{Pd}_3\text{Co}_{950}\text{@CN}$ manufacture has been verified at gram-scale (Fig. S37), which still affords 87.1% HCAL yield and almost identical in-situ DRIFTS spectrum of CO adsorption. Therefore, based on the extremely high substrate tolerance and facile scalability, this study proves that $\text{Pd}_3\text{Co}_{950}\text{@CN}$, as an atomic-level Pd-based material, holds great application potential as a cost-effective multifunctional catalyst.

4. Conclusions

We have successfully prepared $\text{Pd}_x\text{Co}_y\text{@CN}$ with sea-urchin-like morphology by alloying trace Pd in N-rich carbon nanotubes from one-step pyrolysis of ZIF-67@ C_3N_4 , and characterized the obtained catalysts with an array of experimental and theoretical studies, including SEM, TEM/HRTEM, EDS, N_2 adsorption-desorption, XRD, Raman, XPS, XAS, $\text{H}_2\text{-TPR/TPD}$, DRIFTS of CO or CAL, and DFT calculations. Arising from ultra-dilute alloying effect and functional Mott-Schottky heterojunction, the $\text{Pd}_3\text{Co}_{950}\text{@CN}$ catalyst allows efficient electron transfer owing to the atomic-level Pd in PdCo encapsulated within CNT network containing abundant carbon defects and pyridinic N species. The integrated intermetallic and metal-support synergism promotes efficient catalysis in a plurality of hydrogenation and oxidation reactions. With a high specific surface area of $579\text{ m}^2\text{ g}^{-1}$ and low Pd loading of 0.18 wt%, $\text{Pd}_3\text{Co}_{950}\text{@CN}$ shows extraordinary activity in the

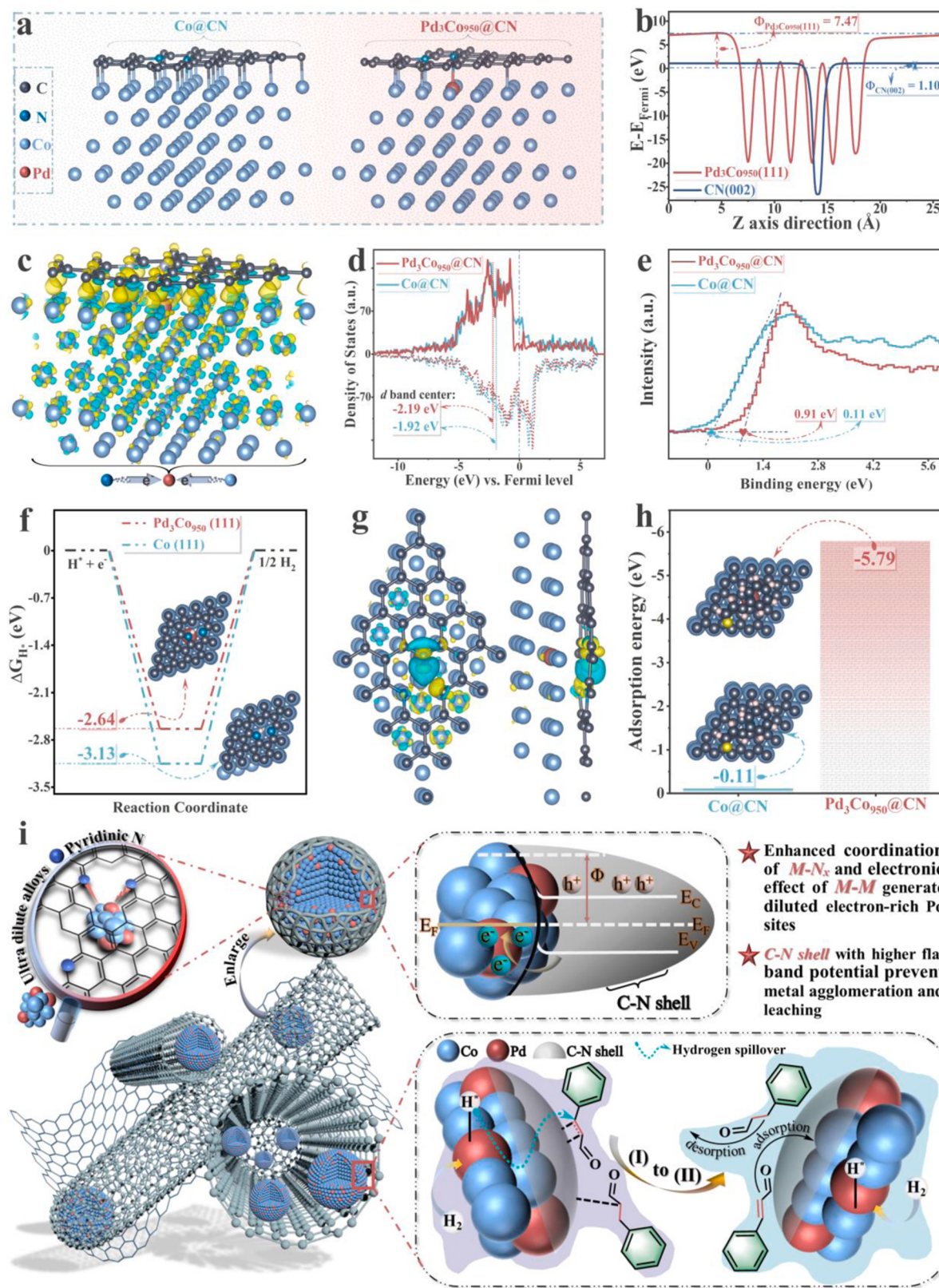
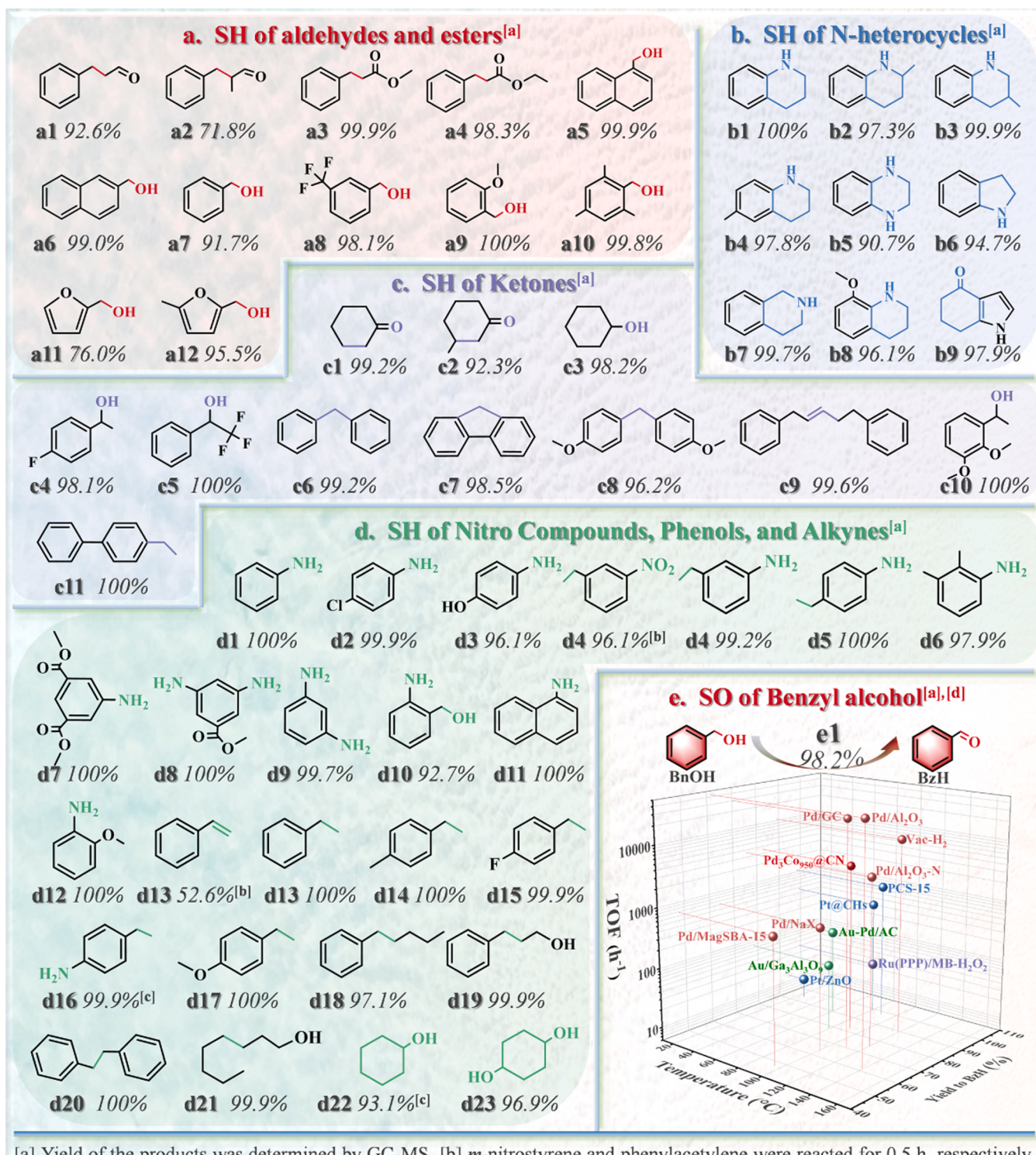


Fig. 5. Theoretical calculations: (a) Geometric configurations of Co (111) and Pd₃Co₉₅₀(111) surfaces. (b) Calculated work function (φ) of Pd₃Co₉₅₀(111) and CN(002) slabs. (c) Differential charge density of Pd₃Co₉₅₀@CN (the yellow and blue regions indicate electron increment and depletion, respectively). (d) PDOS of *d*-bands for Co@CN and Pd₃Co₉₅₀@CN. (e) Valence band spectra of Co@CN and Pd₃Co₉₅₀@CN. (f) Free energies of H adsorption on Co (111) and Pd₃Co₉₅₀(111). (g) Top and side view of charge density difference of H* on the Pd₃Co₉₅₀(111) surface. (h) Adsorption energy of CAL on the surface of Co@CN and Pd₃Co₉₅₀@CN. (i) Proposed mechanism of CAL hydrogenation over Pd₃Co₉₅₀@CN.



[a] Yield of the products was determined by GC-MS. [b] *m*-nitrostyrene and phenylacetylene were reacted for 0.5 h, respectively. [c] *p*-nitroethynylbenzene and phenol as substrate, respectively. [d] Comparison of different catalysts for selective oxidation (SO) of the benzyl alcohol (Red, blue, green, and purple spheres represent Pd, Pt, Au, and Ru, respectively, see Table S5 for details).

Fig. 6. Selective catalysis of various substrates with Pd₃Co₉₅₀@CN.

directional CAL hydrogenation with TOF of 1656 h⁻¹ and HCAL selectivity of 98.9% due to easy hydrogen adsorption/desorption and preferential lay-flat C=C bond activation, outperforming most reported Pd-base catalysts. Thanks to the strong magnetic properties and confinement effect of Pd₃Co₉₅₀ NPs in CNT, the Pd₃Co₉₅₀@CN catalyst exhibits facile recovery, remarkable stability, and excellent scalability.

Gratifyingly, Pd₃Co₉₅₀@CN efficiently catalyzes a broad scope of organic substances with excellent functional group tolerance, indicating universal applicability not only for selective hydrogenation of aldehydes, esters, *N*-heterocycles, ketones, nitro-compounds, phenols, alkynes, but also for selective oxidation of benzyl ethanol. In light of the above findings, the proposed approach offers practical guidelines for

broadening the applications of supported heterogeneous catalysts composed of trace precious metals and base metal hosts.

CRediT authorship contribution statement

Haifeng Yuan: Conceptualization, Methodology, Investigation, Data and formal analysis, Visualization, Writing - original draft, Writing - review & editing. Mei Hong: Data and formal analysis, Data curation, Funding acquisition, Conceptualization, Supervision, Writing - review & editing. Feng Dong and Yanpeng Chen: Investigation, Data and formal analysis, Visualization. Xinjuan Du and Xianzhen Huang: Formal analysis, Data curation. Jinqiang Gao: Formal analysis, Writing - review & editing. Shihe Yang: Formal analysis, Project administration, Funding acquisition, Conceptualization, Supervision, Writing - review & editing. All authors discussed the results, drew conclusions, and commented on the manuscript.

Declaration of Competing Interest

The authors declare that they have no known competing financial interests or personal relationships that could have appeared to influence the work reported in this paper.

Data Availability

Data will be made available on request.

Acknowledgement

This work was financially supported by the National Natural Science Foundation of China (21972006), the Shenzhen Science and Technology Program (JCYJ20200109140421071, JSGG20211029095546003), and Shenzhen Peacock Plan (KQTD2016053015544057).

Appendix A. Supporting information

Supplementary data associated with this article can be found in the online version at [doi:10.1016/j.apcatb.2023.122864](https://doi.org/10.1016/j.apcatb.2023.122864).

References

- [1] H. Zhang, G. Liu, L. Shi, J. Ye, Single-atom catalysts: emerging multifunctional materials in heterogeneous catalysis, *Adv. Energy Mater.* 8 (2018) 1701343, <https://doi.org/10.1002/aenm.201701343>.
- [2] J.D. Lee, J.B. Miller, A.V. Shneidman, L. Sun, J.F. Weaver, J. Aizenberg, J. Biener, J.A. Boscoboinik, A.C. Foucher, A.I. Frenkel, J.E.S. van der Hoeven, B. Kozinsky, N. Marcella, M.M. Montemore, H.T. Ngan, C.R. O'Connor, C.J. Owen, D. J. Stacchiola, E.A. Stach, R.J. Madix, P. Sautet, C.M. Friend, Dilute alloys based on Au, Ag, or Cu for efficient catalysis: from synthesis to active sites, *Chem. Rev.* 122 (2022) 8758–8808, <https://doi.org/10.1021/acs.chemrev.1c00967>.
- [3] J.Q. Wei, J. Wang, W. Shen, Atomically dispersed Fe⁸⁺ anchored on nitrogen-rich carbon for enhancing benzyl alcohol oxidation through Mott-Schottky effect, *Appl. Catal. B: Environ.* 292 (2021), 120195, <https://doi.org/10.1016/j.apcatb.2021.120195>.
- [4] A. Wang, J. Li, T. Zhang, Heterogeneous single-atom catalysis, *Nat. Rev. Chem.* 2 (2018) 65–81, <https://doi.org/10.1038/s41570-018-0010-1>.
- [5] V.M. Chernyshev, V.P. Ananikov, Nickel and palladium catalysis: stronger demand than ever, *ACS Catal.* 12 (2022) 1180–1200, <https://doi.org/10.1021/acscatal.1c04705>.
- [6] T. Zhang, Z. Chen, A.G. Walsh, Y. Li, P. Zhang, Single-atom catalysts supported by crystalline porous materials: views from the inside, *Adv. Mater.* 32 (2020) 2002910, <https://doi.org/10.1002/adma.202002910>.
- [7] R.T. Hannagan, G. Giannakakis, M. Flytzani-Stephanopoulos, E.C.H. Sykes, Single-atom alloy catalysis, *Chem. Rev.* 120 (2020) 12044–12088, <https://doi.org/10.1021/acs.chemrev.0c00078>.
- [8] M.R. Ball, K.R. Rivera-Dones, E.B. Gilcher, S.F. Ausman, C.W. Hullfish, E.A. Lebrón, J.A. Dumescic, AgPd and CuPd catalysts for selective hydrogenation of acetylene, *ACS Catal.* 10 (2020) 8567–8581, <https://doi.org/10.1021/acscatal.0c01536>.
- [9] C.J. Wraxman, A.R. Riscoe, H. Lee, M. Cargnello, Dilute Pd/Au alloys replace Au/TiO₂ interface for selective oxidation reactions, *ACS Catal.* 10 (2020) 1716–1720, <https://doi.org/10.1021/acscatal.9b05227>.
- [10] L. He, F. Weniger, H. Neumann, M. Beller, Synthesis, characterization, and application of metal nanoparticles supported on nitrogen-doped carbon: catalysis beyond electrochemistry, *Angew. Chem. Int. Ed.* 55 (2016) 12582–12594, <https://doi.org/10.1002/anie.201603198>.
- [11] X.-H. Li, M. Antonietti, Metal nanoparticles at mesoporous N-doped carbons and carbon nitrides: functional Mott-Schottky heterojunctions for catalysis, *Chem. Soc. Rev.* 42 (2013) 6593–6604, <https://doi.org/10.1039/C3CS60067J>.
- [12] W. Gong, Y. Lin, C. Chen, M. Al-Mamun, H.-S. Lu, G. Wang, H. Zhang, H. Zhao, Nitrogen-doped carbon nanotube confined Co-N_x sites for selective hydrogenation of biomass-derived compounds, *Adv. Mater.* 31 (2019) 1808341, <https://doi.org/10.1002/adma.201808341>.
- [13] S. Choi, M. Oh, Well-arranged and confined incorporation of PdCo nanoparticles within a hollow and porous metal-organic framework for superior catalytic activity, *Angew. Chem. Int. Ed.* 58 (2019) 866–871, <https://doi.org/10.1002/anie.201812827>.
- [14] X. Wang, K. Maeda, A. Thomas, K. Takanabe, G. Xin, J.M. Carlsson, K. Domen, M. Antonietti, A metal-free polymeric photocatalyst for hydrogen production from water under visible light, *Nat. Mater.* 8 (2009) 76–80, <https://doi.org/10.1038/nmat2317>.
- [15] S. Panić, Á. Kukovecz, G. Boskovic, Design of catalytic carbon nanotube-based reactor for water denitrification - the impact of active metal confinement, *Appl. Catal. B: Environ.* 225 (2018) 207–217, <https://doi.org/10.1016/j.apcatb.2017.11.078>.
- [16] H. Yu, L. Shang, T. Bian, R. Shi, G.L.N. Waterhouse, Y. Zhao, C. Zhou, L.-Z. Wu, C. H. Tung, T. Zhang, Nitrogen-doped porous carbon nanosheets templated from g-C₃N₄ as metal-free electrocatalysts for efficient oxygen reduction reaction, *Adv. Mater.* 28 (2016) 5080–5086, <https://doi.org/10.1002/adma.201670178>.
- [17] X. Zhu, H. Qiu, P. Chen, G. Chen, W. Min, Graphitic carbon nitride (g-C₃N₄) in situ polymerization to synthesize MOF-Co@CNTs as efficient electromagnetic microwave absorption materials, *Carbon* 176 (2021) 530–539, <https://doi.org/10.1016/j.carbon.2021.02.044>.
- [18] W. Zhang, X. Jiang, X. Wang, Y.V. Kaneti, Y. Chen, J. Liu, J.-S. Jiang, Y. Yamauchi, M. Hu, Spontaneous weaving of graphitic carbon networks synthesized by pyrolysis of ZIF-67 crystals, *Angew. Chem. Int. Ed.* 56 (2017) 8435–8440, <https://doi.org/10.1002/anie.201701252>.
- [19] J. Zhang, B. Wang, E. Nikolla, J.W. Medlin, Directing Reaction Pathways through Controlled Reactant Binding at Pd-TiO₂ Interfaces, *Angew. Chem. Int. Ed.* 56 (2017) 6594–6598, <https://doi.org/10.1002/anie.201703669>.
- [20] Z.-D. Yang, X.-Y. Yang, T. Liu, Z.-W. Chang, Y.-B. Yin, X.-B. Zhang, J.-M. Yan, Q. Jiang, In Situ CVD derived Co-N-C composite as highly efficient cathode for flexible Li-O₂ batteries, *Small* 14 (2018) 1800590, <https://doi.org/10.1002/smll.201800590>.
- [21] H. Chen, F. Sun, J. Wang, W. Li, W. Qiao, L. Ling, D. Long, Nitrogen doping effects on the physical and chemical properties of mesoporous carbons, *J. Phys. Chem. C.* 117 (2013) 8318–8328, <https://doi.org/10.1021/jp4017773>.
- [22] H. Chen, K. Shen, Q. Mao, J. Chen, Y. Li, Nanoreactor of MOF-Derived Yolk-Shell Co@C-N: precisely controllable structure and enhanced catalytic activity, *ACS Catal.* 8 (2018) 1417–1426, <https://doi.org/10.1021/acscatal.7b03270>.
- [23] N. Roy, S. Yasmin, A. Ejaz, H. Soon Han, S. Jeon, Influence of pyrrolic and pyridinic-N in the size and distribution behaviour of Pd nanoparticles and ORR mechanism, *Appl. Surf. Sci.* 533 (2020), 147500, <https://doi.org/10.1016/j.apsusc.2020.147500>.
- [24] S.G. Peera, J. Balamurugan, N.H. Kim, J.H. Lee, Sustainable synthesis of Co@NC core shell nanostructures from metal organic frameworks via mechanochemical coordination self-assembly: an efficient electrocatalyst for oxygen reduction reaction, *Small* 14 (2018) 1800441, <https://doi.org/10.1002/smll.201800441>.
- [25] M.J. Islam, M.G. Mesa, A. Osatiashvili, J.C. Manayil, M.A. Isaacs, M.J. Taylor, S. Tsatsos, G. Kyriakou, PdCu single atom alloys supported on alumina for the selective hydrogenation of furfural, *Appl. Catal. B: Environ.* 299 (2021), 120652, <https://doi.org/10.1016/j.apcatb.2021.120652>.
- [26] M. Cheng, P. Lv, X. Zhang, R. Xiong, Z. Guo, Z. Wang, Z. Zhou, M. Zhang, A new active species of Pd-Nx synthesized by hard-template method for efficiently catalytic hydrogenation of nitroarenes, *J. Catal.* 399 (2021) 182–191, <https://doi.org/10.1016/j.jcat.2021.05.016>.
- [27] X. Li, Y. Pan, H. Yi, J. Hu, D. Yang, F. Lv, W. Li, J. Zhou, X. Wu, A. Lei, L. Zhang, Mott-Schottky Effect Leads to Alkyne Semihydrogenation over Pd-Nanocube@N-Doped Carbon, *ACS Catal.* 9 (2019) 4632–4641, <https://doi.org/10.1021/acscatal.9b01001>.
- [28] G. Prieto, A. Martínez, P. Concepción, R. Moreno-Tost, Cobalt particle size effects in Fischer-Tropsch synthesis: structural and in situ spectroscopic characterisation on reverse micelle-synthesised Co/ITQ-2 model catalysts, *J. Catal.* 266 (2009) 129–144, <https://doi.org/10.1016/j.jcat.2009.06.001>.
- [29] Y. Yang, D. Rao, Y. Chen, S. Dong, B. Wang, X. Zhang, M. Wei, Selective hydrogenation of cinnamaldehyde over Co-based intermetallic compounds derived from layered double hydroxides, *ACS Catal.* 8 (2018) 11749–11760, <https://doi.org/10.1021/acscatal.8b02755>.
- [30] W.G. Cui, Y.T. Li, H. Zhang, Z.C. Wei, B.H. Gao, J.J. Dai, T.L. Hu, In situ encapsulated Co/MnO nanoparticles inside quasi-MOF-74 for the higher alcohols synthesis from syngas, *Appl. Catal. B: Environ.* 278 (2020), 119262, <https://doi.org/10.1016/j.apcatb.2020.119262>.
- [31] M. McEntee, A. Stevanovic, W. Tang, M. Neurock, Jhon T. Yates Jr., Electric field changes on Au nanoparticles on semiconductor supports - the molecular voltmeter and other methods to observe adsorbate-induced charge-transfer effects in Au/TiO₂ nanocatalysts, *J. Am. Chem. Soc.* 137 (2015) 1972–1982, <https://doi.org/10.1021/ja511982n>.
- [32] W. Liu, H. Feng, Y. Yang, Y. Niu, L. Wang, P. Yin, S. Hong, B. Zhang, X. Zhang, M. Wei, Highly-efficient RuNi single-atom alloy catalysts toward chemoselective hydrogenation of nitroarenes, *Nat. Commun.* 13 (2022) 3188, <https://doi.org/10.1038/s41467-022-30536-9>.

- [33] G.X. Pei, X.Y. Liu, A. Wang, A. Lee, M.A. Isaacs, L. Li, X. Pan, X. Yang, X. Wang, Z. Tai, K. Wilson, T. Zhang, Ag alloyed Pd single-atom catalysts for efficient selective hydrogenation of acetylene to ethylene in excess ethylene, *ACS Catal.* 5 (2015) 3717–3725, <https://doi.org/10.1021/acscatal.5b00700>.
- [34] J. Chen, K. Giewont, E.A. Walker, J. Lee, Y. Niu, E.A. Kyriakidou, Cobalt-induced PdO formation in low-loading Pd/BEA catalysts for CH₄ oxidation, *ACS Catal.* 11 (2021) 13066–13076, <https://doi.org/10.1021/acscatal.1c00400>.
- [35] H. Wang, X.K. Gu, X. Zheng, H. Pan, J. Zhu, S. Chen, L. Cao, W. Li, J. Lu, Disentangling the size-dependent geometric and electronic effects of palladium nanocatalysts beyond selectivity, *Sci. Adv.* 5 (2019) 6413, <https://doi.org/10.1126/sciadv.aat6413>.
- [36] H. Wang, C. Wang, H. Yan, H. Yi, J. Lu, Precisely-controlled synthesis of Au@Pd core-shell bimetallic catalyst via atomic layer deposition for selective oxidation of benzyl alcohol, *J. Catal.* 324 (2015) 59–68, <https://doi.org/10.1016/j.jcat.2015.01.019>.
- [37] K. Shen, L. Chen, J. Long, W. Zhong, Y. Li, MOFs-templated Co@Pd core-shell NPs embedded in N-doped carbon matrix with superior hydrogenation activities, *ACS Catal.* 5 (2015) 5264–5271, <https://doi.org/10.1021/acscatal.5b00998>.
- [38] G.X. Pei, X.Y. Liu, X. Yang, L. Zhang, A. Wang, L. Li, H. Wang, X. Wang, T. Zhang, Performance of Cu-alloyed Pd single-atom catalyst for semihydrogenation of acetylene under simulated front-end conditions, *ACS Catal.* 7 (2017) 1491–1500, <https://doi.org/10.1021/acscatal.6b03293>.
- [39] M.S. Wilburn, W.S. Epling, Sulfur deactivation and regeneration of mono-and bimetallic Pd-Pt methane oxidation catalysts, *Appl. Catal. B: Environ.* 206 (2017) 589–598, <https://doi.org/10.1016/j.apcatb.2017.01.050>.
- [40] O. Proux, E. Lahera, W.D. Net, I. Kieffer, M. Rovezzi, D. Testemale, M. Irar, S. Thomas, A. Aguilar-Tapia, E.F. Bazarkina, A. Prat, M. Tellà, M. Auffan, J. Rose, J. L. Hazemann, High-energy resolution fluorescence detected x-ray absorption spectroscopy: a powerful new structural tool in environmental biogeochemistry sciences, *J. Environ. Qual.* 46 (2017) 1146, <https://doi.org/10.2134/jeq2017.01.0023>.
- [41] P. Zimmermann, S. Peredkov, P.M. Abdala, S. DeBeer, M. Tromp, C. Müller, J. A. VAM Bokhoven, Modern X-ray spectroscopy: XAS and XES in the laboratory, in: *Coord. Chem. Rev.* 423, 2020, 213466, <https://doi.org/10.1016/j.ccr.2020.213466>.
- [42] H. Sun, H. Jia, D.A. Ramirez-Diaz, N. Budisa, P. Schwille, Fine Tuning. Protein self-organization by orthogonal chemico-optogenetic tools, *Angew. Chem. Int. Ed.* 60 (2021) 1433–7851, <https://doi.org/10.1002/ange.202008691>.
- [43] X. Lan, T. Wang, Highly selective catalysts for the hydrogenation of unsaturated aldehydes: a review, *ACS Catal.* 10 (2020) 2764–2790, <https://doi.org/10.1021/acscatal.9b04331>.
- [44] R. Nie, M. Miao, W. Du, J. Shi, Y. Liu, Z. Hou, Selective hydrogenation of C=C bond over N-doped reduced graphene oxides supported Pd catalyst, *Appl. Catal. B: Environ.* 180 (2016) 607–613, <https://doi.org/10.1016/j.apcatb.2015.07.015>.
- [45] R. Li, W. Yao, Y. Jin, W. Jia, X. Chen, J. Chen, J. Zheng, Y. Hu, D. Han, J. Zhao, Selective hydrogenation of the C=C bond in cinnamaldehyde over an ultra-small Pd-Ag alloy catalyst, *Chem. Eng. J.* 351 (2018) 995–1005, <https://doi.org/10.1016/j.cej.2018.06.146>.
- [46] W. Gong, Y. Lin, C. Chen, M. Al-Mamun, H.-S. Lu, G. Wang, H. Zhang, H. Zhao, Nitrogen-doped carbon nanotube confined Co-N_x sites for selective hydrogenation of biomass-derived compounds, *Adv. Mater.* 31 (2019), <https://doi.org/10.1002/adma.201808341>.
- [47] Z. Li, W. Wei, H. Li, S. Li, L. Leng, M. Zhang, J.H. Horton, D. Wang, W. Sun, C. Guo, W. Wu, J. Wang, Low-temperature synthesis of single palladium atoms supported on defective hexagonal boron nitride nanosheet for chemoselective hydrogenation of cinnamaldehyde, *ACS Nano* 15 (2021) 10175–10184, <https://doi.org/10.1021/acsnano.1c02094>.
- [48] Y. Lv, M. Han, W. Gong, D. Wang, C. Chen, G. Wang, H. Zhang, H. Zhao, Fe-Co alloyed nanoparticles catalyzing efficient hydrogenation of cinnamaldehyde to cinnamyl alcohol in water, *Angew. Chem. Int. Ed.* 59 (2020) 23521–23526, <https://doi.org/10.1002/anie.202009913>.
- [49] J.K. Nørskov, T. Bligaard, B. Hvolbæk, F. Abild-Pedersen, I. Chorkendorff, C. H. Christensen, The nature of the active site in heterogeneous metal catalysis, *Chem. Soc. Rev.* 37 (2008) 2163–2171, <https://doi.org/10.1039/B800260F>.
- [50] S. Li, L. Wang, M. Wu, Y. Sun, X. Zhu, Y. Wan, Measurable surface d charge of Pd as a descriptor for the selective hydrogenation activity of quinoline, *Chinese J. Catal.* 41 (2020) 1337–1347, [https://doi.org/10.1016/S1872-2067\(19\)63580-X](https://doi.org/10.1016/S1872-2067(19)63580-X).
- [51] Q.-G. Wang, L. He, L.-Y. Zhao, R.-S. Liu, W.-P. Zhang, A.-H. Lu, Surface charge-driven nanoengineering of monodisperse carbon nanospheres with tunable surface roughness, *Adv. Funct. Mater.* 30 (2020) 1906117, <https://doi.org/10.1002/adfm.201906117>.
- [52] X. Zhu, Q. Guo, Y. Sun, S. Chen, J.-Q. Wang, M. Wu, W. Fu, Y. Tang, X. Duan, D. Chen, Y. Wan, Optimising surface d charge of AuPd nanoalloy catalysts for enhanced catalytic activity, *Nat. Commun.* 10 (2019) 1428, <https://doi.org/10.1038/s41467-019-09421-5>.
- [53] G. Sun, Z.J. Zhao, R. Mu, S. Zha, L. Li, S. Chen, Ketao Zang, Jun Luo, Z. Li, S. C. Purdy, A.J. Kropf, J.T. Miller, L. Zeng, J. Gong, Breaking the scaling relationship via thermally stable Pt/Cu single atom alloys for catalytic dehydrogenation, *Nat. Commun.* 9 (2018) 4454, <https://doi.org/10.1038/s41467-018-06967-8>.
- [54] W. Zhang, H. Wang, J. Jiang, Z. Sui, Y. Zhu, D. Chen, X. Zhou, Size dependence of Pt catalysts for propane dehydrogenation: from atomically dispersed to nanoparticles, *ACS Catal.* 10 (2020) 12932–12942, <https://doi.org/10.1021/acscatal.0c03286>.
- [55] Y. Lian, T. Fang, Y. Zhang, B. Liu, J. Li, Hydrogenation of CO₂ to alcohol species over Co₃O₄/CN catalysts, *J. Catal.* 379 (2019) 46–51, <https://doi.org/10.1016/j.jcat.2019.09.018>.
- [56] D. Xu, W. Li, H. Duan, Q. Ge, H. Xu, Reaction performance and characterization of Co/Al₂O₃ Fischer-Tropsch catalysts promoted with Pt, Pd and Ru, *Catal. Lett.* 102 (2020) 229–235, <https://doi.org/10.1007/s10562-005-5861-7>.
- [57] Z. Chen, L. Liang, H. Yuan, H. Liu, P. Wu, M. Fu, J. Wu, P. Chen, Y. Qiu, D. Ye, L. Chen, Reciprocal regulation between support defects and strong metal-support interactions for highly efficient reverse water gas shift reaction over Pt/TiO₂ nanosheets catalysts, *Appl. Catal. B: Environ.* 298 (2021), 120507, <https://doi.org/10.1016/j.apcatb.2021.120507>.
- [58] J. Zhang, Z. Gao, S. Wang, G. Wang, X. Gao, B. Zhang, S. Xing, S. Zhao, Y. Qin, Origin of synergistic effects in bicomponent cobalt oxide-platinum catalysts for selective hydrogenation reaction, *Nat. Commun.* 10 (2019) 4166, <https://doi.org/10.1038/s41467-019-11970-8>.
- [59] L. Peng, H. Tian, X. Cui, L. Su, G. Meng, Z. Ma, S. Cao, J. Shi, Dual synergistic catalytic effects boost hydrogen electric oxidation performance of Pd/W₁₈O₄₉, *Nano Res.* 14 (2021) 2441–2450, <https://doi.org/10.1007/s12274-020-3248-0>.
- [60] Y. Tan, X. Liu, L. Zhang, F. Liu, A. Wang, T. Zhang, Producing of cinnamyl alcohol from cinnamaldehyde over supported gold nanocatalyst, *Chin. J. Catal.* 42 (2021) 470–481, [https://doi.org/10.1016/S1872-2067\(20\)63678-6](https://doi.org/10.1016/S1872-2067(20)63678-6).
- [61] H. Wang, Y. Shi, Z. Wang, Y. Song, M. Shen, B. Guo, L. Wu, Selective hydrogenation of cinnamaldehyde to hydrocinnamaldehyde over Au-Pd/ultrathin SnNb₂O₆ nanosheets under visible light, *J. Catal.* 396 (2021) 374–386, <https://doi.org/10.1016/j.jcat.2021.03.011>.
- [62] Z. Jiang, S. Song, X. Zheng, X. Liang, Z. Li, H. Gu, Z. Li, Y. Wang, S. Liu, W. Chen, D. Wang, Y. Li, Lattice strain and schottky junction dual regulation boosts ultrafine ruthenium nanoparticles anchored on a N-modified carbon catalyst for H₂ production, *J. Am. Chem. Soc.* 144 (2022) 19619–19626, <https://doi.org/10.1021/jacs.2c09613>.
- [63] L. Zhao, X. Qin, X. Zhang, X. Cai, F. Huang, Z. Jia, J. Diao, D. Xiao, Z. Jiang, R. Lu, N. Wang, H. Liu, D. Ma, A. Magnetically Separable Pd single - atom catalyst for efficient selective hydrogenation of phenylacetylene, *Adv. Mater.* 34 (2022) 2110455, <https://doi.org/10.1002/adma.202110455>.
- [64] M. Li, Z. Zhao, Z. Xia, M. Luo, Q. Zhang, Y. Qin, L. Tao, K. Yin, Y. Chao, L. Gu, W. Yang, Y. Yu, G. Lu, S. Guo, Exclusive strain effect boosts overall water splitting in PdCu/Ir core/shell nanocrystals, *Angew. Chem. Int. Ed.* 133 (2021) 8324–8331, <https://doi.org/10.1002/ange.202016199>.
- [65] A. Vojvodic, J.K. Nørskov, Optimizing perovskites for the water-splitting reaction, *Science* 334 (2011) 1355–1356, <https://doi.org/10.1126/science.1215081>.
- [66] S. Zhao, Y. Yang, Z. Tang, Insight into structural evolution, active sites, and stability of heterogeneous electrocatalysts, *Angew. Chem. Int. Ed.* 134 (2022) 10186, <https://doi.org/10.1002/ange.202110186>.
- [67] S. He, Z.-J. Shao, Y. Shu, Z. Shi, X.-M. Cao, Q. Gao, P. Hu, Y. Tang, Enhancing metal-support interactions by molybdenum carbide: an efficient strategy toward the chemoselective hydrogenation of α,β-unsaturated aldehydes, *Chem. Eur. J.* 22 (2016) 5698–5704, <https://doi.org/10.1002/chem.201600323>.
- [68] J. Kou, W.D. Wang, J. Fang, F. Li, H. Zhao, J. Li, H. Zhu, B. Li, Z. Dong, Precisely controlled Pd nanoclusters confined in porous organic cages for size-dependent catalytic hydrogenation, *Appl. Catal. B: Environ.* 315 (2022), 121487, <https://doi.org/10.1016/j.apcatb.2022.121487>.
- [69] Z. Wei, F. Shao, J. Wang, Recent advances in heterogeneous catalytic hydrogenation and dehydrogenation of N-heterocycles, *Chin. J. Catal.* 40 (2019) 980–1002, [https://doi.org/10.1016/S1872-2067\(19\)63336-X](https://doi.org/10.1016/S1872-2067(19)63336-X).
- [70] J. Song, Z.-F. Huang, L. Pan, K. Li, X. Zhang, L. Wang, J.-J. Zou, Review on selective hydrogenation of nitroarene by catalytic, photocatalytic and electrocatalytic reactions, *Appl. Catal. B: Environ.* 227 (2018) 386–408, <https://doi.org/10.1016/j.apcatb.2018.01.052>.